Available online at www.sciencedirect.com
ScienceDirect
Geochimica et Cosmochimica Acta 71 (2007) 5804–5820
Geochimica et Cosmochimica Acta
www.elsevier.com/locate/gca

Distribution and speciation of arsenic around roots in a contaminated riparian floodplain soil: Micro-XRF element mapping and EXAFS spectroscopy

Andreas Voegelin *, Frank-Andreas Weber, Ruben Kretzschmar

Soil Chemistry Group, Institute of Biogeochemistry and Pollutant Dynamics, ETH Zurich, CHN, Universitätstrasse 16, 8092 Zurich, Switzerland

Received 13 September 2006; accepted in revised form 9 May 2007; available online 4 September 2007

Abstract

Riparian soils are periodically flooded, leading to temporarily reducing conditions. Diffusion of O_2 through plants into the rhizosphere maintains oxic conditions around roots, thereby promoting trace element fractionation along a redox gradient from the reduced soil matrix towards the oxic rhizosphere. The aim of this study was to determine the distribution and speciation of arsenic around plant roots in a contaminated (170–280 mg/kg As) riparian floodplain soil (gleyic Fluvisol). The analysis of soil thin sections by synchrotron micro-X-ray fluorescence (μ-XRF) spectrometry showed that As and Fe were enriched around roots and that As was closely correlated with Fe. Arsenic contents of three manually separated rhizosphere soil samples from the subsoil were 5–9 times higher than respective bulk As contents. This corresponds to the accumulation of about half of the total As in the subsoil in Fe-enrichments around roots. The speciation of As in the soil was assessed by oxalate extractions at pH 3.0 as well as by X-ray absorption near edge structure (XANES) and extended X-ray fine structure (EXAFS) spectroscopy. More than 77% of the total As was oxalate extractable in all samples. XANES and EXAFS spectra demonstrated that As was predominantly As(V). For the accurate analysis of the EXAFS data with respect to the bonding of As(V) to the Fe- or Al-octahedra of (hydr)oxides and clays, all 3-leg and 4-leg multiple scattering paths within the $As^{(V)}O_4$-tetrahedron were considered in a fully constrained fitting scheme. We found that As(V) was predominantly associated with Fe-(hydr)oxides, and that sorption to Al- and Mn-hydroxides was negligible. The accumulation of As in the rhizosphere may affect As uptake by plants. Regarding the mobility of As, our results suggest that by oxygenation of the rhizosphere, plants attenuate the leaching of As from riparian floodplain soils during periods of high groundwater levels or flooding.

1. INTRODUCTION

Riparian floodplains are sensitive ecosystems that play a key role in the transfer of nutrients and contaminants between surface and ground water (Kirk, 2004). Anthropogenic emissions from mining and smelting, agriculture and industry have led to the accumulation of heavy metals and arsenic in riparian floodplain soils in industrialized regions worldwide. Even if the source of the contamination has been eliminated, accumulated contaminants in floodplain soils may still represent a continuing risk for surface and ground water quality (Kalbitz and Wennrich, 1998; Lamers et al., 2006). In addition, they may also adversely affect soil fertility and ecosystem health through their uptake by soil organisms and plants and their transfer along the food chain (Vink, 2002; Wijnhoven et al., 2006).

Arsenic is a redox-sensitive trace element and its fate in the environment strongly depends on its oxidation state and speciation. Inorganic As species usually prevail in soils, unless they were contaminated with organic arsenical pesticides. In oxic to mildly reducing soils, inorganic arsenic is predominantly present as the pentavalent oxyanion arsenate (As(V)) or the trivalent oxyanion arsenite (As(III)). As-sulfides may form in strongly reducing systems

* Corresponding author. Fax: +41 44 633 11 18.
E-mail address: voegelin@env.ethz.ch (A. Voegelin).

0016-7037/$ - see front matter © 2007 Elsevier Ltd. All rights reserved.
doi:10.1016/j.gca.2007.05.030

(Inskeep et al., 2002). As(III) is considered to have a higher acute toxicity than As(V) (Penrose, 1974). Over the typical pH range of soil solutions, arsenite ($pK_1 = 9.1$, $I = 0.1$ M, Martell et al., 1997) is mainly present as a neutral undissociated species (H_3AsO_3), while arsenate ($pK_1 = 2.8$, $pK_2 = 6.7$, $pK_3 = 11.8$, $I = 0.1$ M, Martell et al., 1997) is present as a singly ($H_2AsO_4^-$) or doubly ($HAsO_4^{2-}$) deprotonated anion. Laboratory studies demonstrate that Fe-oxides, Al-oxides, Mn-oxides, and clay minerals are effective sorbents for As(III) and As(V) in soils (Fuller et al., 1993; Scott and Morgan, 1995; Goldberg, 2002; Violante and Pigna, 2002; Waltham and Eick, 2002; Foster et al., 2003; Ona-Nguema et al., 2005). While both As(V) and As(III) strongly sorb to Fe-(hydr)oxides (Goldberg, 2002; Dixit and Hering, 2003), As(V) more effectively competes for sorption sites than As(III) in the presence of anions such as phosphate or silicate (Roberts et al., 2004). Because of the high affinity of As for Fe-(hydr)oxides (Pierce and Moore, 1982), the cycling of As in floodplain soils is closely related to the cycling of Fe.

Under waterlogged conditions, the microbial decomposition of organic matter leads to the depletion of O_2 and to the reductive dissolution of Fe-(hydr)oxides in soils (Ponnamperuma, 1972). Adsorbed As(III) and As(V) are concomitantly released into soil solution and As(V) gets reduced to As(III) (Masscheleyn et al., 1991; McGeehan and Naylor, 1994; Onken and Hossner, 1996). While deeper soil horizons may be permanently waterlogged and reduced, fluctuations of the water table closer to the soil surface may cause the redox potential to vary between oxidizing and reducing conditions. However, even under waterlogged conditions, the diffusion of O_2 through plant roots into the surrounding soil matrix may keep the rhizosphere soil oxidized (Kirk, 2004). At the same time, transpiration water flow and diffusion lead to the transport of dissolved Fe^{2+} from the reduced soil matrix towards the roots. These processes result in the oxidation of Fe^{2+} and precipitation of Fe(III)-(hydr)oxides on the surface of roots (Fe-plaque) and in the surrounding oxidized rhizosphere soil (Otte et al., 1995; Doyle and Otte, 1997; Caetano and Vale, 2002; Kirk, 2004). The redistribution of Fe between the soil matrix and the rhizosphere also affects the distribution of As (Otte et al., 1995; Doyle and Otte, 1997; Hansel et al., 2002; Blute et al., 2004; Liu et al., 2004a,b; Hu et al., 2005).

Studies on the sequestration of As in the rhizosphere of plants grown in contaminated salt-marshes showed a significant enrichment of As in the rhizosphere soil around roots and in Fe-plaque on the root surface (Otte et al., 1995; Doyle and Otte, 1997; Caetano and Vale, 2002). Recent synchrotron-based microspectroscopic studies showed that the Fe-plaque of *Typha latifolia* (broadleaf cattail) and *Phalaris arundinacea* (reed canarygrass) was mainly composed of ferrihydrite and minor fractions of goethite and siderite (Hansel et al., 2001, 2002; Blute et al., 2004). Arsenic at the root surface was found to be predominantly As(V) associated with the Fe-plaque, and Fe-plaque was suggested to cause an attenuation of the As mobility (Hansel et al., 2002; Blute et al., 2004). In the context of the irrigation of rice fields in Bangladesh and West Bengal with As-rich groundwater and the potential accumulation of As in paddy soils, recent studies suggest that the formation of Fe-plaque on the surface of rice roots reduces the As(V) transfer into the paddy rice plants (Liu et al., 2004a,b, 2006; Chen et al., 2005; Hu et al., 2005).

Previous microspectroscopic studies on the spatial distribution of As focused on the Fe-plaque on the root surface (Hansel et al., 2002; Blute et al., 2004). In this study, we investigated soil thin sections by micro-X-ray fluorescence spectrometry (μ-XRF) to determine the distribution of As, Fe, and Mn between the soil matrix and the rhizosphere around roots in a contaminated riparian floodplain soil. The extent of As accumulation in the rhizosphere was quantified by the analysis of manually separated rhizosphere and matrix soil. To characterize the reactivity and speciation of As in the rhizosphere and in the soil matrix, we used oxalate extractions and X-ray absorption spectroscopy (XAS). For the determination of the sorption mode of As in soils using extended X-ray absorption fine structure (EXAFS) spectroscopy, we developed a robust fitting approach for the distinction between As(V) bonding to the Al- and Fe-octahedra of Al- and Fe-bearing sorbents.

2. EXPERIMENTAL

2.1. Sampling site

The studied riparian floodplain is located at the river Mulde near Muldenstein (Saxony-Anhalt, Germany). It is subject to occasional flooding (Brandt, 2003; Klemm et al., 2005). The contamination at the site mainly results from past mining activities 150 km upstream in the Ore Mountains (Erzgebirge), where sulfide ores have been mined for centuries for Ag, Pb, and Zn. The ongoing erosion and weathering of mine tailings and acid mine drainage still lead to substantial particulate and dissolved contaminant loads in the Mulde and to the widespread contamination of adjacent floodplains (Klemm et al., 2005). Following the centennial flood of the rivers Mulde and Elbe in summer 2002, a detailed monitoring has been performed to determine the extent of the environmental contamination along the two rivers (Geller et al., 2004). An extensive study of the distribution and dynamics of contaminants in floodplains near Muldenstein has been carried out previously (Brandt, 2003). The soil profile studied in the present work is located at about 15 m distance from the river close to profile #2 on transect #1 in Brandt's report. The soil is classified as a gleyic Fluvisol according to the *World Reference Base for Soil Resources* (FAO, 2006a,b). The vegetation is dominated by perennial grasses (*Calamagrostis epigejos*, wood small reed; *P. arundinacea*, reed canarygrass) and flowering plants (e.g., *Cirsium arvense*, creeping thistle; *Arctium minus*, lesser burdock; *Heracleum sphondylium*, hogweed; *Artemisia vulgaris*, mugwort; *Urtica dioica*, stinging nettle).

2.2. Soil samples

Bulk soil samples were collected in January 2004 from three soil depths (0–15 cm, 20–40 cm, and 70–80 cm). The samples were air dried, sieved to less than 2 mm, and stored

in plastic containers in the dark for further analyses. Undisturbed samples for the preparation of soil sections were collected from two soil depths (10–15 cm and 40–45 cm) in October 2004 using Kubiena boxes (8 cm × 6 cm × 5 cm). Within 3 days after sampling, the undisturbed soil was frozen by immersion in liquid N_2 and subsequently freeze dried. The dried samples were embedded using LR White® resin (London Resin, Reading, UK) under vacuum and subsequently cured for 48 h at 60 °C in an 800 mbar N_2 atmosphere. Sections of 300 μm thickness were cut using a diamond saw. Polished sections were mounted on As-free glass slides and ground and polished to 30 μm thin sections (Labor Beckmann, Schwülper-Lagesbüttel, Germany). Due to the lower organic carbon content of the subsoil, Fe-enrichments around plant roots could be visually discerned from the soil matrix based on their rusty color. From an undisturbed block of soil collected with a Kubiena box at 40–45 cm depth (total weight 157 g), 6.6 g of this Fe-rich material (subsequently termed "rhizosphere soil") and 10.6 g of the matrix soil were manually separated. Subsequently, the rhizosphere soil, the matrix soil, and the remaining soil material were homogenized and ball-milled to <50 μm for further analyses. The element concentrations in the total soil volume were calculated from their concentrations in the three isolates (rhizosphere, matrix, and rest) and the weights of these isolates. The same procedure was applied to two additional blocks of undisturbed soil collected in January 2004 using Kubiena boxes. These samples were from 30 to 35 cm (total weight 239 g) and 45–50 cm depth (total weight 179 g). At both sampling dates, the soil profile was dry and well aerated down to at least 1.5 m.

2.3. Bulk chemical analyses

The pH of the sieved soil samples was measured in 10 mM $CaCl_2$ using a glass electrode. Powdered samples <50 μm were obtained using an agate ball-mill. The content of organic carbon was determined on powdered samples using a CHNS Analyzer (LECO CHNS-932). Wax pellets were prepared from the powdered samples (4 g of soil and 0.9 g of wax) and analyzed for total element contents by energy dispersive X-ray fluorescence spectrometry (Spectro X-Lab 2000). For the determination of oxalate extractable element contents, 0.2 M oxalate solution with pH 3.0 was prepared by adding 0.2 M $(NH_4)C_2O_4$ to 0.2 M $H_2C_2O_4$ until pH 3.0 was reached. In triplicates, 200 mg of soil were weighed into 10 mL PE tubes and extracted with 10 mL of oxalate solution (4 h, dark). After centrifugation (15 min at 3500*g*), the solutions were filtered through 0.2 μm nylon filters and acidified with 1% (v/v) 30% HCl (Suprapure). The extracts were analyzed by inductively coupled plasma—optical emission spectrometry (ICP-OES, Varian Vista-MPX).

2.4. Reference samples for X-ray absorption spectroscopy

For the preparation of reference samples of As(III) and As(V) adsorbed to 2-line ferrihydrite, a method for the synthesis of 2-line ferrihydrite (Schwertmann and Cornell, 1991) was slightly modified. About 66 mL of 1 M KOH were slowly added to 100 mL of 0.2 M $Fe(NO_3)_3{\cdot}9\,H_2O$ solution without exceeding pH 8. When the pH reached 5.5, i.e., after addition of about 65 mL of 1 M KOH, the titration was briefly interrupted. Fifty milliliters of either 0.012 M $Na_2HAsO_4{\cdot}7H_2O$ or 0.012 M $NaAsO_2$ (molar ratio As/Fe = 4/100) were rapidly mixed to the freshly precipitated ferrihydrite before finalizing the titration with 1 M KOH to pH 7. After the endpoint of the titration was reached, the samples were centrifuged and the supernatant decanted. The ferrihydrite was washed and centrifuged twice using doubly deionized water (18.2 MΩcm, Milli-Q® Element, Millipore). Subsequently, the samples were rapidly frozen by immersion of the containers in liquid N_2 and subsequently freeze dried. Reference samples for As(III) and As(V) adsorbed to hydrous Al oxide (HAO) were synthesized in analogy to As(III) and As(V) adsorbed to ferrihydrite using $Al(NO_3)_3{\cdot}9H_2O$ instead of $Fe(NO_3)_3{\cdot}9H_2O$. Scorodite ($Fe^{III}As^{V}O_4{\cdot}H_2O$) was synthesized by adapting a method for the synthesis of variscite (Hsu and Sikora, 1993). Thirty milliliters of 0.5 M Na_2HAsO_4 were mixed with 50 mL of 1 M HCl and 100 mL doubly deionized water. Subsequently, 20 mL of 0.5 M $FeCl_3{\cdot}6H_2O$ were rapidly added. The precipitate was aged for 9 days at 90 °C and then washed and freeze dried as described above for ferrihydrite. The crystalline structure of the references was verified by powder X-ray diffraction analysis (D4 Endeavour, Bruker AXS).

For analysis by Fe K-edge EXAFS spectroscopy, ferrihydrite and goethite were synthesized according to (Schwertmann and Cornell, 1991). Synthetic lepidocrocite was kindly provided by Paul Borer, ETH Zurich, Switzerland (Borer et al., 2005).

2.5. Collection and extraction of X-ray absorption spectra

Arsenic K-edge X-ray absorption near edge structure (XANES) and extended X-ray absorption fine structure (EXAFS) spectra were measured at the X-ray absorption spectroscopy (XAS) beamline at the Angströmquelle Karlsruhe (ANKA, Karlsruhe, Germany). The ring was operated at 2.5 GeV with a beam current of 130 mA. For the reduction of the higher harmonics, the Si(1 1 1) monochromator was detuned by 35% using a software-controlled monochromator stabilization. The energy resolution of the Si(1 1 1) monochromator at the As K-edge was approximately 2.3 eV. This resolution did not allow to resolve sharp features in the XANES region, but was sufficient for EXAFS analysis (Foster et al., 2003). The monochromator was calibrated using an Au-foil (first maximum of the first derivative of the Au L3-edge XANES spectrum at 11919 eV). Powdered soil samples were mixed with a small amount of polyethylene powder and pressed as 13-mm pellets. The pellets were analyzed at room temperature in fluorescence mode using a 5-element Ge solid state detector. Powdered reference samples were diluted with polyethylene powder and prepared as 13-mm pellets for analysis in transmission mode. Three scans were collected from soil samples and 2 scans from references. Each scan took about 90 min. Extraction of normalized XANES and EXAFS spectra from the raw data was performed using the software

code Athena (Ravel and Newville, 2005). The E_0 was determined from the maximum of the first derivative of the measured signal. Normalized spectra were obtained by fitting a first order polynomial to the data up to 30 eV below the edge and a second order polynomial to the data from 150 eV to 450–500 eV above the edge. EXAFS spectra were extracted using the Autobk algorithm implemented in Athena ($R_{bkg} = 0.8$; k-weight = 3, spline k-range from 0.5 $Å^{-1}$ upwards). For shell fits, Fourier-transformed EXAFS spectra were extracted over k-ranges from 3 to 11.5–13.5 $Å^{-1}$, using a Kaiser–Bessel apodization window (window parameter = 2.5).

Fe K-edge EXAFS spectra of reference samples and one rhizosphere soil sample were collected using the same setup as for As K-edge measurements. The monochromator was calibrated using an Fe-foil (maximum of first derivative at 7112 eV). For the references, E_0 was obtained from the maximum of the first inflection point. The XANES spectrum of the rhizosphere soil sample appeared distorted by pinholes in the sample pellet (Manceau and Gates, 1997), resulting in a shift of the maximum of the first derivative to a value below the effective E_0. The E_0 for this spectrum was therefore fixed to the one of ferrihydrite. EXAFS spectra were extracted from the experimental data using the Autobk algorithm ($R_{bkg} = 0.9$; k-weight = 3; k-range 0.5–10.5 $Å^{-1}$). Fourier transforms were calculated over the k-range 2–10 $Å^{-1}$ using a Kaiser–Bessel apodization window (window parameter = 2.5).

2.6. XAS data analysis

The As K-edge EXAFS data were analyzed by shell fits on the Fourier-transformed EXAFS signal (k-range 3 to 11.5–13.5 $Å^{-1}$, r-range 0.8–3.6 Å) using the software code Artemis (Ravel and Newville, 2005). Theoretical single and multiple scattering EXAFS paths were calculated from the structure of scorodite (Kitahama et al., 1975) using FEFF 8.2 (Ankudinov and Rehr, 2000). In the analysis of spectra of As(V) reference samples and of soil samples (which contained mostly As(V)), we considered As–O and As–Fe single scattering (SS) paths and multiple scattering (MS) paths within the $As^{(V)}O_4$-tetrahedron with at most 4 legs. A SS As–Al path was calculated by replacing Fe by Al in the scorodite structure. Three types of MS were included into fits: triangular As–O–O (MS1, 3 legs, degeneracy = 12), collinear As–O–As–O (MS2, 4 legs, degeneracy = 4), and non-collinear As–O–As–O (MS3, 4 legs, degeneracy = 12). Due to the distortion of the $As^{(V)}O_4$-tetrahedron in scorodite (Kitahama et al., 1975), FEFF calculations resulted in 4 individual As–O single scattering paths, 6 two-fold degenerated MS1 paths, 4 MS2 paths, and 6 two-fold degenerated MS3 paths. In test calculations, we used all individual paths for one specific type of MS and calculated their composite EXAFS signal fixing the Debye–Waller parameter (σ^2) and E_0 of all paths to 0.005 $Å^2$ and 0 eV, respectively. We then used each individual path to fit the composite signal by adjusting half path length R, Debye–Waller parameter σ^2 and energy shift E_0 while fixing the degeneracy to the theoretical value (12 for MS1, 4 for MS2, and 12 for MS3). These tests showed that using the path whose half path length was closest to the average half path length of all individual paths resulted in the most accurate fit for the average half path length, σ^2 and E_0. Thus, for all shell fits, we used the As–O, MS1, MS2, and MS3 path whose half path length was closest to the average half path length of all individual paths of the same type of scattering. While the degeneracies of the MS paths were fixed to their theoretical value, their half path lengths were expressed as a function of the SS As–O half path length assuming an ideal tetrahedron. Thus, the half path lengths of the paths MS2 and MS3 were set to twice the As–O SS half path length, and the half path length of the MS1 path to 1.8165 ($=1+\sqrt{(2/3)}$) times the As–O SS half path length.

The Debye–Waller parameters for the MS paths were constrained by considering the correlation between the lengths of individual legs (Hudson et al., 1996). Because the collinear As–O–As–O path (MS2) involves twice the same O atom, the first As–O–As half path length and the second As–O–As half path length (each equal to the As–O SS distance) are fully correlated. Therefore, we defined the σ^2 for the half path length of the MS2 path to be four times the σ^2 of the As–O SS path. In contrast, the non-collinear As–O–As–O path (MS3) involves two different O atoms. Therefore, the first As–O–As half path length and the second As–O–As half path length were assumed to be uncorrelated. Consequently, the σ^2 for the half path length of the MS3 path was defined to be two times the σ^2 of the As–O SS distance. Assuming that the lengths of the As–O and the O–As leg of the triangular As–O–O (MS1) path are not correlated, their contribution to the σ^2 of MS1 half path length equals half the σ^2 of the As–O SS path. However, because also the O–O leg contributes to the σ^2 of the MS1 path, we assumed the σ^2 of the MS1 path to be equal to the σ^2 of the As–O SS path.

For shell fits of As(III) adsorbed to ferrihydrite, only the triangular As–O–O MS path was considered. While its degeneracy was fixed to the theoretical value of 6, its σ^2 was assumed to be equal to the σ^2 of the As–O SS, and its half path length was adjusted.

Linear combination fits (LCF) were performed on the soil EXAFS spectra over the k-range 3–11 $Å^{-1}$ using the reference spectra of As(V) and As(III) adsorbed to ferrihydrite as proxies for soil As(V) and As(III), respectively. For LCF, the EXAFS data were extracted using the same E_0 (11,871 eV) and Autobk spline k-range (0.5–11.5 $Å^{-1}$) for all spectra. The sum of the fitted fractions was not constrained and no energy shift was included in the LCF. Because the energy resolution (~2.3 eV) of the Si(1 1 1) monochromator used for this work was relatively low and because LCF on the XANES spectra is more strongly affected by small differences in energy calibration (<0.2 eV) than LCF on the EXAFS data, we did not assess As oxidation state based on LCF of the XANES spectra.

2.7. Micro-X-ray fluorescence spectrometry

The spatial distribution of As, Fe, Mn and other elements in soil thin sections from the topsoil (10–15 cm) and the subsoil (40–45 cm) was analyzed by micro-X-ray

fluorescence (μ-XRF) spectrometry at beamline 10.3.2 at the Advanced Light Source (ALS, Berkeley, USA) (Marcus et al., 2004a). Soil sections were mounted in a 45° angle to the incident beam, and the fluorescence signal was recorded in a 90° angle using a Ge 7-element solid state detector. Mapping for As and Fe was carried out at either 12,985 or 12,500 eV incident photon energy using a beam size of 20×20 μm^2 and step sizes of 15 μm in the x- and y-direction. For the distribution of Mn in the topsoil, an additional map was collected at 7012 eV incident photon energy (100 eV below the Fe K-edge) at the same spatial resolution and step width. For the subsoil sample, the Mn Kα intensity was recorded at 12,985 eV incident photon energy. The scatter plot of the Mn intensity versus the Fe intensity for all pixels of the subsoil map exhibited a sharp lower limit which linearly increased with Fe intensity, indicating that leakage of Fe Kα fluorescence into the Mn channel was proportional to the recorded Fe signal. Therefore, the Mn signal of each pixel was decontaminated by subtracting a constant fraction of the recorded Fe signal of the respective pixel. This fraction was determined graphically from the scatter plot of the Mn intensity versus the Fe intensity.

3. RESULTS AND DISCUSSION

3.1. Characterization of the soil profile

Bulk soil properties and total and oxalate extractable contents of Fe, Mn, Al, and As are listed in Table 1. The soil is acidic throughout the profile. In the year 1996, soil pH values at this site were between 5.8 and 6.0 down to 120 cm depth. The groundwater level was at approximately 80 cm depth and was regulated by a weir 600 m downstream (Brandt, 2003). In 2004, when soil samples were collected for this study, the weir was open and the groundwater table at both sampling dates was below the maximum profile depth of ~150 cm. The soil pH value of 4.3 in our sample from 70 to 80 cm depth (Table 1) might therefore result from oxidation processes that occurred after the weir had been opened and the previously waterlogged subsoil was exposed to air. The humus-rich topsoil Ah horizon is of uniform color and extends to 20 cm depth. It is sharply separated from the underlying subsoil Blc horizon. The first few cm of the subsoil are compacted and the root density in the subsoil is markedly lower than in the Ah horizon. The clear separation between Ah and Blc horizon and the compaction of the first few cm of the Blc horizon may result from agricultural use of the site before 1980. All soil samples have silt loam texture. Within the soil profile, however, also sandy layers were present reflecting the alluvial origin of the soil material. Fluctuations in the water table and occasional flooding result in redoximorphic features in the subsoil (>20 cm). Blackish Fe/Mn mottles occur in the soil matrix, while massive concentric Fe-enrichments with reddish to yellowish color are present around plant roots. Especially around large roots, a blackish rim is sometimes present between the root and the reddish-yellowish Fe-enrichments, indicating the presence of Mn-oxides closest to the root surface. In the topsoil, redoximorphic features are less strongly developed and masked by the color of the soil organic matter. From the Ah horizon to the Blc2 horizon, the oxalate extractable contents of Fe, Mn, and Al decrease (Table 1). The soil is contaminated with As and other trace elements such as Pb, Cu, Cd, and Zn at levels far above geogenic background concentrations. The As concentrations reported in this study (Table 1) compare well to concentrations of 3.43 mmol/kg at 0–17 cm depth, 4.97 mmol/kg at 17–37 cm depth, and 2.07 mmol/kg at 37–100 cm depth reported in a previous study for the size fraction <63 μm (Brandt, 2003). According to the latter study, As contamination extends to at least 2.7 m depth. At 0–15 cm depth, As is almost completely oxalate extractable (Table 1). At 70–80 cm depth, oxalate extractable As accounts for ~80% of the total As. The lower oxalate extractable fraction at that depth may be due to the lower total As content (Table 1), assuming that the soil material contains some As in recalcitrant primary minerals and that the content of these phases does not vary greatly with profile depth.

Table 1
Physicochemical properties and total and oxalate extractable contents of As, Fe, Mn, and Al in the soil samples from three sampling depths

Sampled soil horizon	Ah	Blc	Blc2
Depth (cm)	0–15	20–40	70–80
pH ($CaCl_2$)	5.5	5.7	4.3
Org. C (g/kg)	87.5	48.4	7.8
Sand/silt/clay (g/kg)	200/580/220	170/580/250	270/580/150
Total (mmol/kg)			
As_{tot}	3.38	3.66	2.22
Fe_{tot}	674	712	539
Mn_{tot}	14.0	14.1	11.5
Al_{tot}	1956	2542	2378
Oxalate extractable (mmol/kg (% of total))			
As_o	3.29 (97%)	3.31 (91%)	1.80 (81%)
Fe_o	221 (33%)	197 (28%)	95.7 (18%)
Mn_o	10.8 (77%)	12.4 (88%)	3.77 (33%)
Al_o	241 (12%)	133 (5.2%)	29.3 (1.2%)

3.2. Element mapping in the soil matrix and the rhizosphere by μ-XRF

To determine the sequestration of Fe, Mn, and As between the soil matrix and Fe-enrichments around plant roots in situ, thin sections prepared from undisturbed topsoil (10–15 cm) and subsoil (40–45 cm) were analyzed by μ-XRF. The distribution of As, Fe, and Mn around a root channel in the subsoil is depicted in Fig. 1. Note that the root itself is not visible, because freeze drying led to shrinking of the roots to small fragments. The root channel is located at the top left corner and is oriented perpendicular to the section (Fig. 1). Fe is clearly enriched up to a distance of about 1 mm around the root, but can also be observed at lower concentrations in the soil matrix. In contrast to Fe, Mn is only enriched in concretions close to the root surface. Arsenic is clearly enriched around the root channel compared to the distant soil matrix and its distribution closely

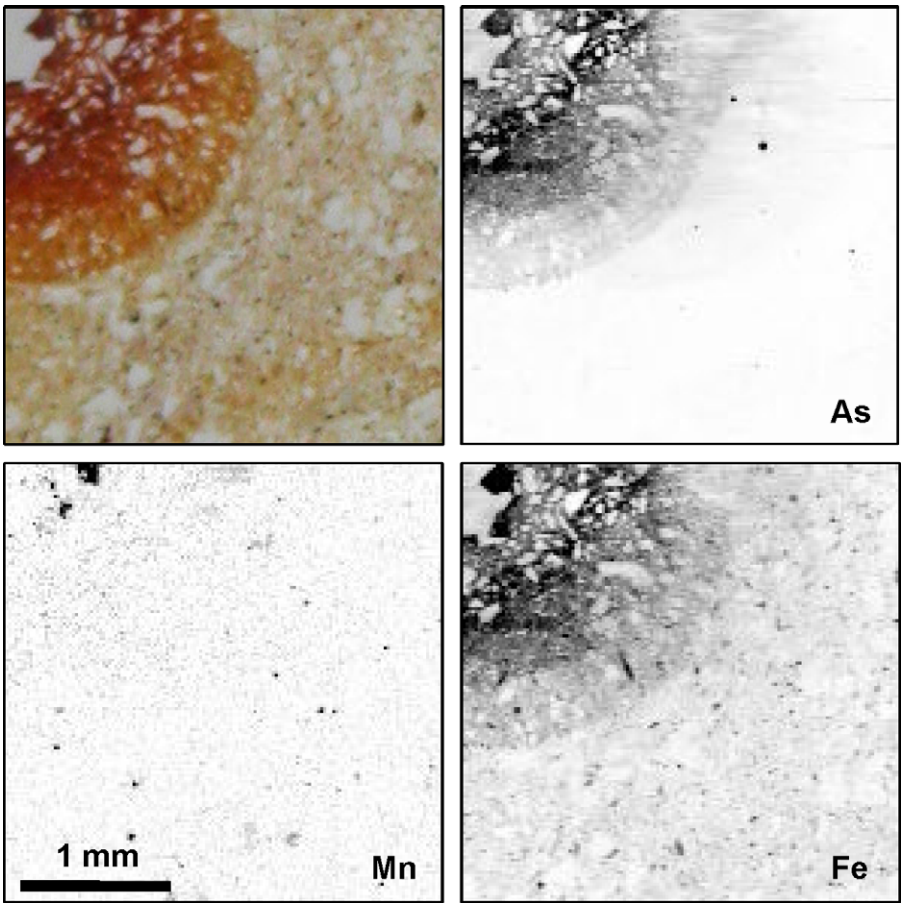

Fig. 1. Distribution of As, Fe, and Mn around a root in the subsoil (40–45 cm depth). The light microscope image (top left) shows the Fe-enriched rhizosphere extending about 1 mm from the root channel, which runs perpendicular to the section in the top left corner (white area). The As, Fe, and Mn maps were recorded at an incident photon energy of 12,985 eV (white corresponds to zero counts per pixel, white-black scale covers intensity range accounting for 95% of cumulative counts of all pixels). As and Fe are enriched around the root channel. Highest concentrations are found at about 0.5 mm from the channel surface. Mn is enriched in concretions close to the channel surface.

matches the distribution of Fe around the root channel. The highest As and Fe concentrations occur at a distance of about 0.5 mm from the root.

In Fig. 2, the distribution maps for As, Fe, and Mn around a root in the topsoil are shown. In this thin section, a root channel extents from left to right almost in the plane of the section. At the left side of the section, the root channel was cut at a flat angle (white oval area in light microscope image). Like in the subsoil, Fe is highly enriched around the root and As closely follows the distribution pattern of Fe. The highest enrichment of As and Fe is observed in a sharp front away from the root channel, in agreement with the distribution observed around the root channel in the subsoil. An area enriched in Mn is observed between the As/Fe-enrichment front and the root channel surface, like in the subsoil.

3.3. Total and oxalate-extractable As, Fe, Mn, and Al in the rhizosphere and Fe speciation by EXAFS spectroscopy

While the elemental distribution maps (Figs. 1 and 2) indicate that As is highly enriched around plant roots in close correlation with Fe, the μ-XRF data do not allow for an accurate quantification of the degree of As, Fe, and Mn accumulation in the rhizosphere. The low content of organic substance in the subsoil and the formation of cemented Fe/Mn-enriched crusts around plant roots allowed manually separating the Fe-enriched soil around plant roots (rhizosphere soil) from the soil matrix (non-rhizosphere soil). The total and oxalate extractable contents of As, Fe, Mn, and Al in such isolates obtained from an undisturbed soil sample collected at 40–45 cm depth are listed in Table 2. The total contents clearly reflect the general findings from the element distribution maps (Figs. 1 and 2): Both Fe and Mn are enriched in the rhizosphere soil. More than nine times higher As concentrations were found in the rhizosphere than in the bulk soil, in qualitative agreement with the element distribution in the subsoil thin section (Fig. 1). Based on the Fe contents of the bulk soil (Fe_{bulk}), the rhizosphere soil (Fe_{rhizo}), and the matrix soil (Fe_{matrix}), we estimated that the rhizosphere soil accounts for about 9% of the mass of the investigated undisturbed soil sample ($Fe_{bulk} = R \times Fe_{rhizo} + (1 - R) \times Fe_{matrix}$, R being the mass fraction of rhizosphere soil). Based on this estimate, about 72% of the total As in the investigated soil block (total mass 157 g) was calculated to be contained in the Fe-enriched

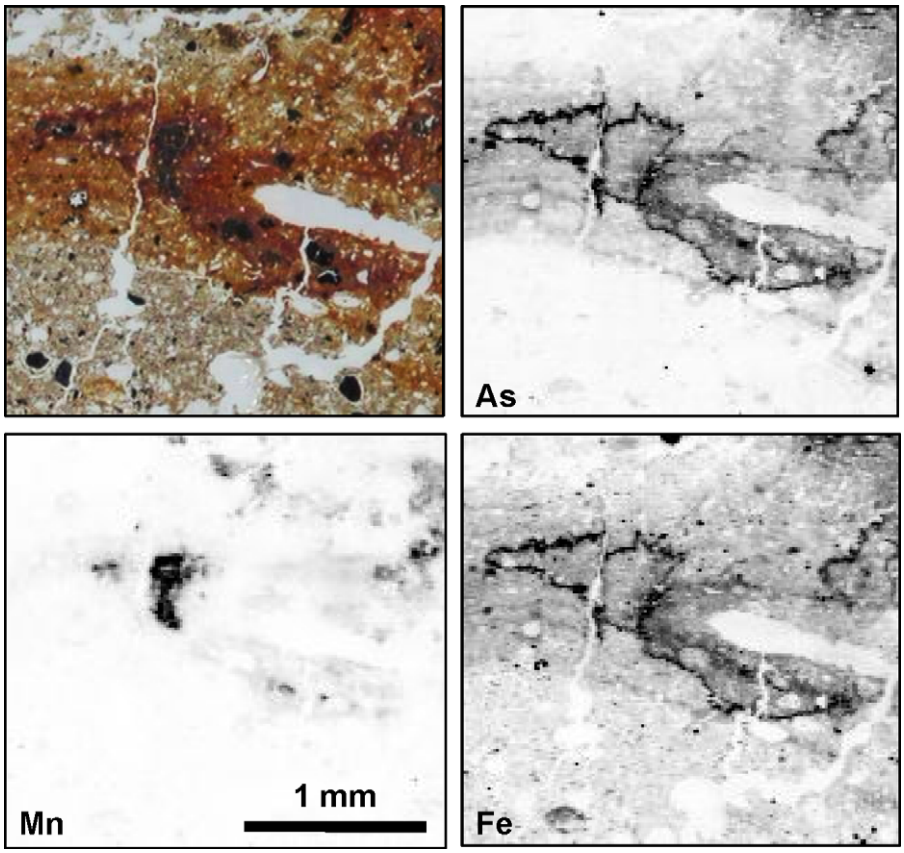

Fig. 2. Distribution of As, Fe, and Mn around a root in the topsoil (10–15 cm depth). The light microscope image (top left) shows the Fe-enriched zone around a root channel, which runs almost in the plane of the section. At the right side of the slide, the channel was cut at a flat angle (white oval area). The As and Fe maps were recorded at 12,985 eV and the Mn map at 7012 eV incident photon energy (white corresponds to zero counts per pixel, white-black scale covers intensity range accounting for 95% of cumulative counts of all pixels). Arsenic is closely associated with Fe near the root channel. The highest concentrations are observed in a rim at some distance from the channel surface. A large Mn-concretion is located close to the root channel.

Table 2
Total and oxalate extractable contents of As, Fe, Mn, and Al in soil material from 40–45 cm depth (bulk), the manually separated Fe-enriched rhizosphere soil and the soil matrix

Sample	Bulk	Rhizosphere	Matrix
Total (mmol/kg)			
As_{tot}	3.66	33.5	1.30
Fe_{tot}	487	1383	398
Mn_{tot}	11.8	40.7	7.54
Al_{tot}	2221	1699	2279
Oxalate extractable (mmol/kg (% of total))			
As_o	3.23 (88%)	29.7 (88%)	1.00 (77%)
Fe_o	116 (24%)	860 (62%)	40.1 (10%)
Mn_o	6.67 (57%)	33.6 (83%)	3.04 (40%)
Al_o	23.5 (1.1%)	30.7 (1.8%)	27.2 (1.2%)

rhizosphere. From two blocks of undisturbed soil collected in January 2004 from 30 to 35 cm (total mass 179 g) and 45–50 cm depth (total mass 239 g), As contents of 22.9 and 16.1 mmol/kg were determined in the Fe-enriched rhizosphere, in comparison to bulk As contents of 4.3 and 3.4 mmol/kg, respectively. Thus, the As concentrations in these samples were about five times higher than in the bulk soil. Assuming that the Fe-enriched rhizosphere soil accounted for 9% of the total soil volume, rhizosphere As was estimated to account for 48% and 42% of the total As in the investigated soil volumes, respectively. Thus, the data suggest that a substantial fraction of As in the rooted subsoil is associated with Fe-enrichments around plant roots. However, the calculated fractions are associated with considerable uncertainty due to the limited soil volumes studied. On the other hand, the results clearly demonstrate that As concentrations in the rhizosphere may largely exceed bulk As contents in the soil.

Only 10% of the Fe in the soil matrix was oxalate extractable (Table 2), indicating that most Fe is contained in primary minerals, clay minerals, and crystalline Fe-(hydr)oxides. In contrast, most of the Fe in the rhizosphere soil was oxalate extractable, suggesting Fe enrichment in readily soluble Fe(III)-(hydr)oxides. In Fig. 3, the Fourier-transformed EXAFS spectrum of the rhizosphere soil is compared to the reference spectra of lepidocrocite, goethite, and ferrihydrite. The differences in the second shell peaks of the reference phases are due to the different numbers of corner and edge-sharing Fe-octahedra in their structure (Manceau and Combes, 1988; Waychunas et al., 1993). The EXAFS spectrum from the rhizosphere soil closely resembles the ferrihydrite spectrum, indicating that ferrihy-

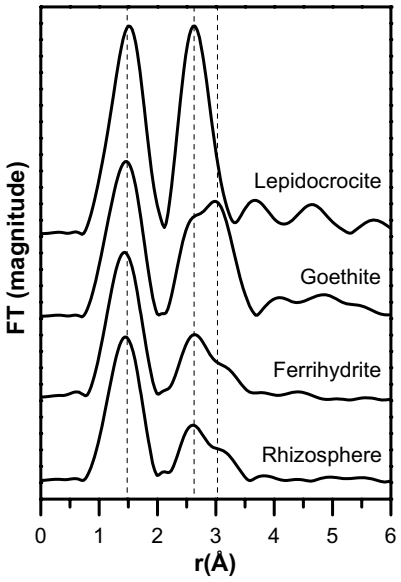

Fig. 3. Fourier-transformed Fe K-edge EXAFS spectra of references and rhizosphere soil (not corrected for phase shift). The dashed vertical lines at 1.5, 2.65, and 3.05 Å indicate the approximate positions of peaks arising from the backscattering contributions of first shell O, second shell edge-sharing Fe, and second shell corner-sharing Fe, respectively.

drite was the dominant Fe species in the rhizosphere soil sample. This finding is in agreement with previous studies (Hansel et al., 2001, 2002) and with the high fraction of oxalate extractable Fe in the rhizosphere soil (Table 2).

Most As in the rhizosphere and the matrix soil was extracted by oxalate, suggesting that it was predominantly associated with poorly crystalline Fe-hydroxides (Wenzel et al., 2001). Alternatively, As might also be adsorbed to Al- and Mn-(hydr)oxides (Arai et al., 2001; Goldberg and Johnston, 2001; Goldberg, 2002; Foster et al., 2003; Beaulieu and Savage, 2005). However, considering the molar amounts of Fe, Mn, and Al extracted from the rhizosphere soil relative to the molar amount of extracted As (Table 2), it is likely that ferrihydrite and other Fe(III)-(hydr)oxides were the dominant sorbents for As in the rhizosphere. In order to corroborate this interpretation, we used As K-edge XANES and EXAFS spectroscopy to characterize the oxidation state and speciation of As in the soil samples.

3.4. Speciation of As in soil samples by XANES spectroscopy

In Fig. 4, the XANES spectra of (A) reference compounds and (B) bulk soil samples are shown. The reference spectra of As(V)- and As(III)-compounds differ in the position of their white line (11870.2 eV and 11873.5 eV, respectively). The white line positions of the spectra collected on soil samples closely match the white line position of the As(V)-references, indicating that As(V)-compounds dominate As speciation in the soil samples. The spectrum of As(V) adsorbed to ferrihydrite resembles published XANES spectra of similar reference materials (Cancès et al., 2005). In contrast to the spectrum of As(V) adsorbed to ferrihydrite, the spectrum of As(V) adsorbed to hydrous aluminum oxide (HAO) exhibits a second maximum around 11890 eV. This feature is also present in published XANES spectra for As(V) adsorbed to gibbsite or bayerite (Foster et al., 1998; Arai et al., 2001; Ladeira et al., 2001; Manning, 2005). Compared to the spectrum of As(V) adsorbed to ferrihydrite, the spectrum of scorodite is more structured in the extended XANES region and its white line is reduced in height, in agreement with published spectra of As(V)-sorbed goethite and scorodite (Foster et al., 1998). With respect to these differences, the spectra of the soil samples most closely resemble the spectrum of As(V) adsorbed to ferrihydrite.

3.5. Shell fitting of the EXAFS spectrum of As(V) adsorbed to ferrihydrite

Because of the similarity of soil XANES spectra with the spectrum of As(V) adsorbed to ferrihydrite (Fig. 4), the EXAFS spectrum of this reference was used to set up a fit model for soil EXAFS spectra. Preliminary fits showed that ~2 Fe atoms could be fit at an As–Fe distance of ~3.3 Å. In studies on As(V) sorption to ferrihydrite, goethite, lepidocrocite, and hematite, this distance has been assigned to bidentate As(V) sorption complexes in which the $As^{(V)}O_4$-tetrahedron shares corners with the apices of two edge-sharing Fe octahedra (Waychunas et al., 1993; Fendorf et al., 1997; Foster et al., 1998; O'Reilly et al., 2001; Farquhar et al., 2002; Arai et al., 2004). Because of the strong correlation between Debye–Waller parameter and coordination number of the As–Fe path, the As–Fe coordination number was fixed to 2 in further fits of the spectrum of As(V) adsorbed to ferrihydrite, i.e., to the coordination number of the predominant bidentate corner-sharing complex. These fits are shown in Fig. 5. Respective fit parameters are listed in Table 3. The fit including only the As–O and As–Fe single scattering paths (Fig. 5, spectrum a) deviates from the experimental data in the lower k-range (peak between 4 and 5.5 $Å^{-1}$) and does not match all details of the second-shell peak in r-space (2–3.5 Å). In previous studies, triangular As–O–O multiple scattering was included to improve the quality of shell fits (Foster et al., 1998; Morin et al., 2002; Paktunc et al., 2003; Sherman and Randall, 2003; Beaulieu and Savage, 2005; Cancès et al., 2005). In the present study, we considered all three types of 3- and 4-leg MS within the $As^{(V)}O_4$-tetrahedron using a fully constrained fit model (see Section 2 and Table 3 for details). As shown in Table 3, the sequential addition of the triangular As–O–O (MS1), the collinear As–O–As–O (MS2), and the non-collinear As–O–As–O (MS3) path each led to an incremental decrease of the R-factor (normalized sum of squared residuals). Since the MS paths were added without increasing the number of adjustable parameters, also the reduced χ^2 (Stern et al., 1995) decreased, suggesting that the fit model effectively improved. In Fig. 5, it can be seen that both the match to the EXAFS spectrum in the k-range 4–5.5 $Å^{-1}$ and the Fourier transform in the r-range 2–3.5 Å improved. On the other hand, the addition of the MS paths did not substantially affect the fit results for the As–O and As–Fe SS paths (Table 3).

In order to assess the sensitivity of EXAFS fits for distinction between As(V) bonding to Al- and Fe-octahedra, we also

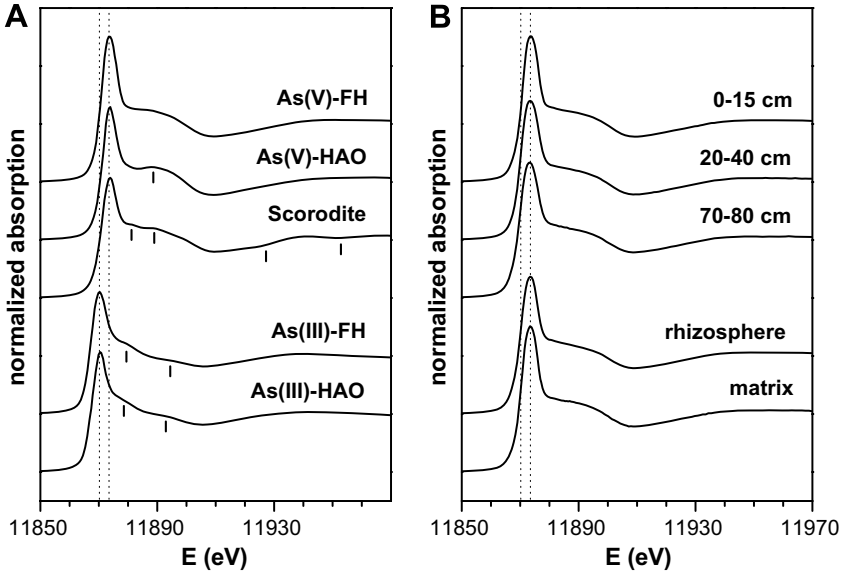

Fig. 4. (A) As K-edge XANES spectra of reference samples. The references include As(V) adsorbed to ferrihydrite and hydrous Al oxide (As(V)–FH and As(V)–HAO, respectively), scorodite ($Fe^{III}As^{V}O_4 \cdot H_2O$), and As(III) adsorbed to ferrihydrite and hydrous Al oxide (As(III)–FH and As(III)–HAO, respectively). The vertical dashed lines at 11870.2 and 11873.5 eV indicate the approximate positions of the white lines of As(III)- and As(V)-compounds. Short vertical bars mark specific features in the reference spectra. (B) As K-edge XANES spectra of soil samples from 0–15 cm, 40–45 cm, and 70–80 cm depth and of rhizosphere and matrix soil isolated from an undisturbed block of soil from 40–45 cm depth.

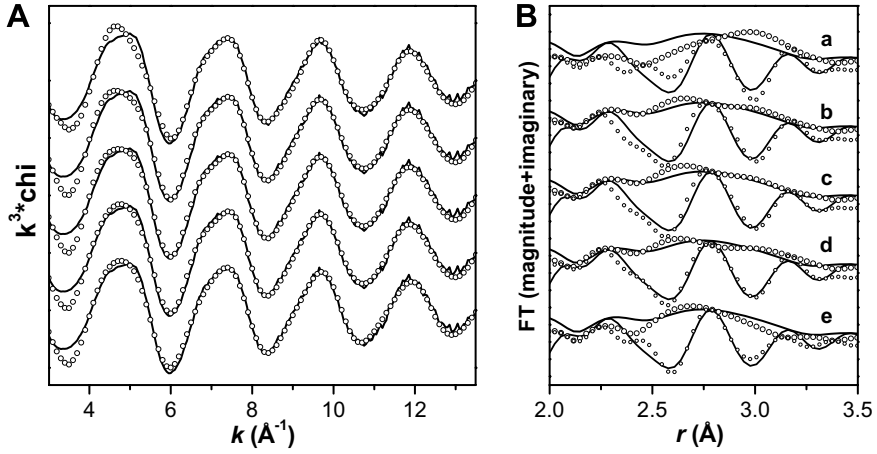

Fig. 5. Shell fits (open dots) of the EXAFS spectrum of As(V) adsorbed on ferrihydrite (solid lines) are shown in (A) *k*-space and (B) over the *r*-range of the second shell and multiple scattering contributions. Paths used in the fits (in addition to As–O) are: (a) As–Fe, (b) As–Fe + MS1, (c) As–Fe + MS1 + MS2, (d) As–Fe + MS1 + MS2 + MS3, and (e) As–Al. Corresponding fit parameters are listed in Table 3.

fitted the spectrum of As(V) adsorbed to ferrihydrite with an As–O and an unrealistic As–Al SS path. Surprisingly, this fit was far better than the one using the As–O and As–Fe SS paths, both in terms of its match to the experimental data in the lower *k*-range and in *r*-space as well as in terms of its *R*-factor (Fig. 5, spectra a and e, Table 3). The fitted As–Al distance of 3.14 Å is similar to distances of 3.11–3.14 Å reported for As(V) adsorbed to hydrated γ-Al_2O_3 (Arai et al., 2001; Arai and Sparks, 2002). Thus, a better fit to the spectrum of As(V) adsorbed to ferrihydrite was obtained with Al than Fe as second neighbor atom. This effect could lead to erroneous conclusions with respect to the speciation of As(V) in unknown samples based on EXAFS analysis. The reason for this misleading fit result is demonstrated in Fig. 6, which shows the combination of the As–Fe and multiple scattering EXAFS signal as well as its individual components compared to the EXAFS of the As–Fe and the As–Al path alone. Multiple scattering contributes significantly to the EXAFS signal in the lower *k*-range, explaining the improvement in the EXAFS fit achieved by its addition (Fig. 5, spectra a–d, Table 3). Comparing the signal of the As–Fe or the As–Al SS path to the combination of the As–Fe SS and the MS paths shows that in the lower *k*-range, where the EXAFS signal from the second shell is most intense, the As–Al path yields a better fit to the combined signal than the As–Fe path alone (Fig. 6, spectra e and f, respec-

Table 3
Shell fits of the spectrum of As(V) adsorbed to ferrihydrite using single- and multiple-scattering paths

Fit	Path	N[a]	R[b] (Å)	σ^2[c] (Å^2)	ΔE_0[d]	R-factor[e]	Red. χ^2[f]
Fe	As–O	4.05	1.69	0.0026	13.3	0.0222	96
	As–Fe	**2**	3.31	0.0103			
Fe + MS1	As–O	4.07	1.69	0.0026	13.1	0.0194	84
	As–Fe	**2**	3.31	0.0116			
	MS1[g]	**12**	3.07	0.0026			
Fe + MS1 + MS2	As–O	4.06	1.69	0.0026	13.4	0.0171	74
	As–Fe	**2**	3.31	0.0116			
	MS1[g]	**12**	3.07	0.0026			
	MS2[h]	**4**	3.38	0.0103			
Fe + MS1 + MS2 + MS3	As–O	4.03	1.69	0.0025	13.7	0.0149	64
	As–Fe	**2**	3.31	0.0113			
	MS1[g]	**12**	3.07	0.0025			
	MS2[h]	**4**	3.38	0.0102			
	MS3[i]	**12**	3.38	0.0051			
Al	As–O	4.03	1.69	0.0026	13.7	0.0166	72
	As–Al	**2**	3.14	0.0060			
Al + MS1	As–O	4.06	1.69	0.0026	13.4	0.0212	92
	As–Al	**2**	3.16	0.0077			
	MS1[g]	**12**	3.07	0.0026			
Al + MS1 + MS2	As–O	4.08	1.69	0.0026	13.6	0.0214	93
	As–Al	**2**	3.15	0.0085			
	MS1[g]	**12**	3.07	0.0026			
	MS2[h]	**4**	3.38	0.0105			
Al + MS1 + MS2 + MS3	As–O	4.07	1.69	0.0026	13.7	0.0197	86
	As–Al	**2**	3.14	0.0084			
	MS1[g]	**12**	3.07	0.0026			
	MS2[h]	**4**	3.38	0.0105			
	MS3[i]	**12**	3.38	0.0052			

The fitted spectra are shown in Fig. 5 and contributions from individual paths are compared in Fig. 6. The number of adjustable variables was 6 and the number of independent datapoints 18.4 in all fits.

[a] Degeneracy (coordination number for single scattering paths), uncertainty for As–O ± 0.29–0.35, values in bold were fixed during shell fitting (see text for details), amplitude reduction factor $S_0^2 = 1$.

[b] Half path length (inter-atomic distance for single scattering paths), uncertainty for As–O ± 0.003–0.005 Å, for As–Fe ± 0.023–0.027 Å, for As–Al ± 0.019–0.033 Å.

[c] Debye–Waller parameter, uncertainty for As–O ± 0.0005–0.0006 Å^2, for As–Fe ± 0.0026–0.0031 Å^2, for As–Al ± 0.0022–0.0039 Å^2.

[d] Energy shift constrained to same value for all paths in fit, uncertainty $<\pm 1.5$ eV.

[e] Normalized sum of the squared residuals of the fit ($R = \sum(\text{data-fit})^2/\sum\text{data}^2$).

[f] Reduced χ^2 (Stern et al., 1995).

[g] MS1 = triangular As–O–O MS path, degeneracy = 12, $R = 1.8165 \times R_{\text{As–O}}$, $\sigma^2 = \sigma^2_{\text{As–O}}$.

[h] MS2 = collinear As–O–As–O MS path, degeneracy = 4, $R = 2 \times R_{\text{As–O}}$, $\sigma^2 = 4 \times \sigma^2_{\text{As–O}}$.

[i] MS3 = non-collinear As–O–As–O MS path, degeneracy = 12, $R = 2 \times R_{\text{As–O}}$; $\sigma^2 = 2 \times \sigma^2_{\text{As–O}}$.

tively). In the higher k-range, the As–Fe path better matches the combined signal (As–Fe + MS). However, because the contribution from the second shell to the EXAFS decreases with increasing k-value, paralleled by an increase in experimental noise, the As–Al path overall yields a better match to the combined signal (As–Fe + MS) than the As–Fe path alone. However, if all three MS paths were added to the fit using the As–Al path, the quality of the fit deteriorated and became worse than the respective fit with the As–Fe path (Table 3). Thus, MS paths need to be included in EXAFS fits in order to differentiate between bidentate corner-sharing As(V) bonding to Al- or Fe-octahedra based on the goodness of the fit. A similar conclusion was drawn in a previous study (Beaulieu and Savage, 2005), though without testing the fit model on EXAFS spectra of reference samples. We also tested our fit model on the spectrum of As(V) adsorbed to hydrous aluminum oxide (HAO) (fits not shown). In this case, the fit with the As–Al path was clearly better than the one with the As–Fe path, with or without addition of the MS paths. This suggests that if MS is ignored in fits of EXAFS spectra of samples with unknown As(V) speciation, it is more likely that contributions from Fe second neighbors are misinterpreted to result from Al neighbors than vice versa.

3.6. EXAFS spectra of As(V) adsorbed to hydrous aluminum oxide, scorodite, and As(III) adsorbed to ferrihydrite

The reference spectra of As(V) adsorbed to HAO, scorodite, and As(III) adsorbed to ferrihydrite are shown in Fig. 7 (spectra g, h, and i, respectively). The correspond-

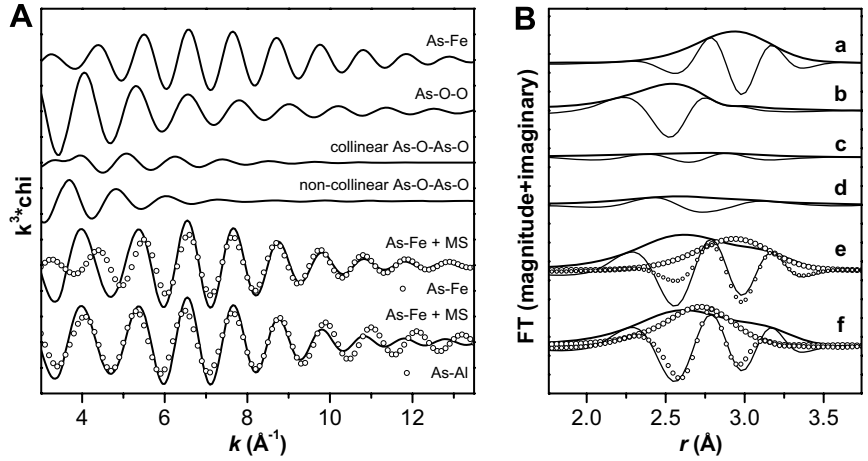

Fig. 6. Interference of single and multiple scattering paths used to fit the second shell of As(V) adsorbed to ferrihydrite. (A) Comparison of the spectra of single and multiple scattering paths in *k*-space and (B) in *r*-space. (a) As–Fe path, (b) triangular As–O–O path (MS1), (c) collinear As–O–As–O path (MS2), (d) non-collinear As–O–As–O path (MS3), (e) combination of As–Fe + MS1 + MS2 + MS3 (solid line) compared to the As–Fe path (open dots), (e) combination of As–Fe + MS1 + MS2 + MS3 (solid line) compared to the As–Al path (open dots). The paths As–Fe and the MS paths are from fit "Fe+MS1+MS2+MS3" and the As–Al path from the fit "Al" reported in Table 3.

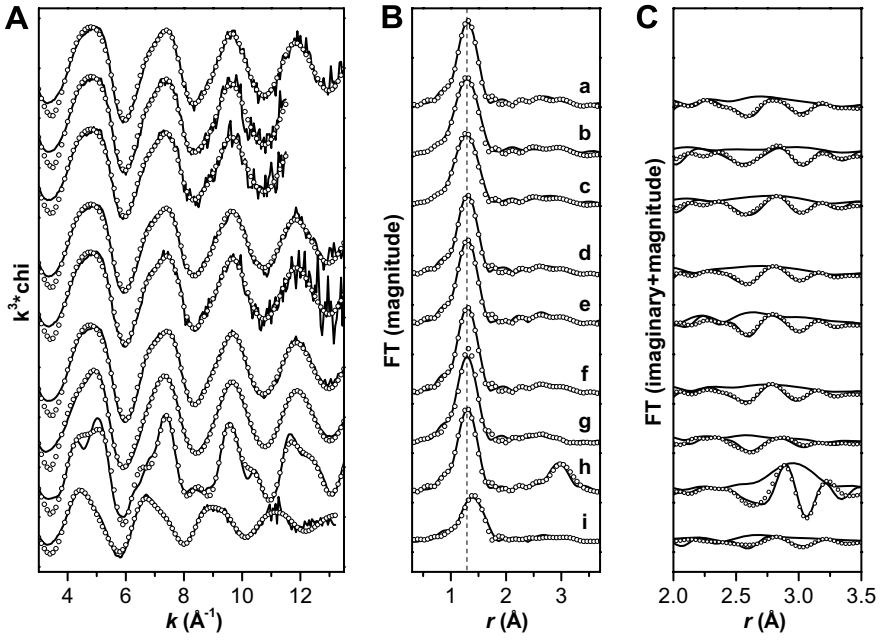

Fig. 7. (A) EXAFS spectra (solid lines) and shell fits (open dots) of soil and reference samples. (B) Fourier transform magnitudes (solid lines) and shell fits (open dots). (C) Imaginary parts and magnitudes of the Fourier transform in the *r*-range 2–3.5 Å (solid lines) and shell fits of the imaginary part (open dots). Samples: (a) Soil 0–15 cm, (b) soil 20–40 cm, (c) soil 70–80 cm, (d) rhizosphere soil 40–45 cm, (e) matrix soil 40–45 cm, (f) As(V) adsorbed to ferrihydrite, (g) As(V) adsorbed to hydrous aluminum oxide, (h) scorodite, (i) As(III) adsorbed to ferrihydrite. Parameters of the shell fits are reported in Table 4.

ing fit parameters are listed in Table 4. The spectrum of As(V) adsorbed to HAO was fit in analogy to the spectrum of As(V) adsorbed to ferrihydrite. The As–Al distance of 3.21 ± 0.03 Å compares to As–Al distances of 3.19 ± 0.05 Å (Ladeira et al., 2001) and 3.16 ± 0.03 Å (Foster et al., 1998) reported for As(V) adsorbed to gibbsite. For scorodite, the coordination number of the As–Fe path was fixed to the crystallographic value of 4. The fitted As–Fe distance of 3.38 ± 0.01 Å corresponds to reported values (3.36–3.37 Å) from EXAFS and X-ray diffraction analyses (Kitahama et al., 1975; Foster et al., 1998; O'Reilly et al., 2001; Paktunc et al., 2003). The As–O distance of 1.79 ± 0.01 Å for As(III) adsorbed to ferrihydrite is typical for As(III) coordinated to 3 O atoms, and the As–Fe distance of 3.38 ± 0.04 Å is similar to the dominant distance of 3.40–3.41 Å previously reported for As(III) adsorbed to ferrihydrite (Ona-Nguema et al., 2005).

Table 4
Structural characterization of As in the soil samples and in reference compounds by shell fitting in *r*-space using theoretical paths

Sample	Path	N[a]	R[b] (Å)	σ^{2}[c] (Å^2)	ΔE_0[d]	R-factor[e]	Red. χ^2[f]
Soil 0–15 cm	As–O	3.93	1.69	0.0023	13.8	0.0141	14
	As–Fe	1.92	3.34	**0.0113**[h]			
	MS1 + MS2 + MS3[g]						
Soil 20–40 cm	As–O	3.99	1.69	0.0025	14.5	0.0240	15
	As–Fe	2.07	3.36	**0.0113**[h]			
	MS1 + MS2 + MS3[g]						
Soil 70–80 cm	As–O	3.82	1.69	0.0028	13.5	0.0205	11
	As–Fe	1.85	3.34	**0.0113**[h]			
	MS1 + MS2 + MS3[g]						
Rhizosphere 40–45 cm	As–O	3.69	1.69	0.0024	13.7	0.0146	37
	As–Fe	1.67	3.33	**0.0113**[h]			
	MS1 + MS2 + MS3[g]						
Soil matrix 40–45 cm	As–O	3.90	1.69	0.0024	13.2	0.0158	6
	As–Fe	2.07	3.32	**0.0113**[h]			
	MS1 + MS2 + MS3[g]						
As(V) on ferrihydrite	As–O	4.03	1.69	0.0025	13.7	0.0149	64
	As–Fe	**2**[i]	3.31	0.0113			
	MS1 + MS2 + MS3[g]						
As(V) on HAO	As–O	4.12	1.69	0.0023	12.4	0.0104	381
	As–Al	**2**[i]	3.21	0.0098			
	MS1 + MS2 + MS3[g]						
Scorodite	As–O	3.79	1.68	0.0022	12.3	0.0283	808
	As–Fe	**4**[j]	3.38	0.0070			
	MS1 + MS2 + MS3[g]						
As(III) on ferrihydrite	As–O	3.07	1.79	0.0046	18.5	0.0385	27
	As–Fe	1.00	3.38	**0.0100**			
	As–O–O	**6**[j]	3.17	0.0046[k]			

The fits are shown in Fig. 7.
[a] Degeneracy (coordination number for single scattering paths), uncertainty for As–O ± 0.26–0.47, for As–Fe/Al 0.6–1.0, values in bold were fixed during shell fitting, amplitude reduction factor $S_0^2 = 1$.
[b] Half path length (inter-atomic distance for single scattering paths), uncertainties are ~0.01 Å for As–O, 0.02–0.04 for As–Fe and As–Al.
[c] Debye–Waller parameter, uncertainties for As–O are 0.0005–0.0010 Å^2, values in bold were fixed during shell fitting.
[d] Energy shift constrained to same value for all paths in fit, uncertainties 0.1–1.8 eV.
[e] Normalized sum of the squared residuals of the fit ($R = \sum(\text{data-fit})^2/\sum\text{data}^2$).
[f] Reduced χ^2 (Stern et al., 1995).
[g] Multiple scattering paths MS1, MS2, and MS3 fully constrained (see text and Table 3 for details).
[h] Fixed to value obtained for As(V) adsorbed to ferrihydrite.
[i] Fixed to coordination number of bidentate corner sharing complex.
[j] Fixed to theoretical values.
[k] Constrained to equal $\sigma^2_{\text{As–O}}$.

3.7. Speciation of As in soil samples by EXAFS spectroscopy

The EXAFS spectra of the soil samples together with model fits are shown in Fig. 7, the corresponding fit parameters are provided in Table 4. In analogy to the final fit of As(V) adsorbed to ferrihydrite, all three types of multiple scattering within the $As^{(V)}O_4$-tetrahedron were included. For the As–Fe path, the Debye–Waller parameter was fixed to the value obtained for As(V) adsorbed to ferrihydrite, while the coordination number was optimized in the fits. The fitted As–O distances of 1.69 ± 0.01 Å are typical for adsorbed As(V) and As(V)-bearing minerals, as seen for adsorbed As(V) and scorodite. In contrast, As(III)–O distances are higher, as reflected by the As–O distance of 1.79 Å for As(III) adsorbed to ferrihydrite (Table 4). Thus, the As–O distances fitted to the soil spectra suggest that As in the samples is mainly As(V). For all studied soil samples, good fits were obtained using an As–Fe path. Using an As–Al path instead resulted in fits of significantly lower quality. If an As–Al path was fit in addition to the As–Fe path, the residual χ^2 of the fit increased, and the fit returned unrealistic As–Al distances and coordination numbers. Thus, we conclude from the EXAFS spectra that As(V) in the studied soil samples is predominantly associated with Fe-bearing phases and that bonding to Al-oxides or Al-octahedra at the edges of clay minerals is negligible. This interpretation is in agreement with the close correlation of Fe and As in the element distribution maps (Figs. 1 and 2), with the interpretation of the oxalate extractions (Tables 1 and 2), and the comparison of the XANES spectra from soil samples

with those of As(V) adsorbed to ferrihydrite and hydrous aluminum oxide (Fig. 4). These findings compare to the results of a recent study on As speciation in a soil contaminated with lead arsenate (Cancès et al., 2005) in which the authors concluded that most As(V) was adsorbed to Fe-(hydr)oxides rather than Al-(hydr)oxides or clays.

In the shell fits, we focused on the distinction between As(V) binding to Al- and Fe-bearing phases. Due to the similarity of their scattering amplitudes, distinction between Fe and Mn second neighbors located at the same distance from the absorbing atom would be difficult. However, reported As–Mn distances for As(V) adsorbed the birnessite and vernadite cover the range from 3.15 to 3.22 Å (Foster et al., 2003; Manning et al., 2002). These As–Mn distances are significantly shorter than the As–Fe distance of As(V) adsorbed to ferrihydrite and the As–Fe distances fitted to the soil spectra (Table 4). In *k*-space, the shorter As–Mn distances of As(V) adsorbed to hydrous Mn oxides result in a pronounced beat pattern at about 7 $Å^{-1}$ (Manning et al., 2002; Foster et al., 2003), which is absent in the spectrum of As(V) adsorbed to ferrihydrite and in the soil As spectra (Fig. 7). Thus, the EXAFS data show that As(V) adsorption to Mn(IV)-(hydr)oxides is quantitatively not relevant, in agreement with the lack of As–Mn correlations in the element distribution maps (Figs. 1 and 2).

The As–O distances and coordination numbers obtained for soil EXAFS spectra indicated that most soil As was As(V) (Table 4). In order to estimate the fraction of As(III) in the soil samples, we performed linear combination fits (LCF) over the *k*-range 3–11 $Å^{-1}$ using the spectra of As(V) and As(III) adsorbed to ferrihydrite as proxies for soil As(V) and As(III) (Table 5). One-component fits based on the spectrum of As(V) adsorbed to ferrihydrite indicated that only the soil from 70–80 cm depth and the rhizosphere sample contained significantly less than 100% As(V). For these two samples, addition of the spectrum of As(III) adsorbed to ferrihydrite substantially improved the fits, as judged by the decrease of the *R*-factor by 10% or more (Table 5). Examination of the Fourier-transformed LCF spectra of the other soil samples showed that addition of the As(III) reference also led to a visually better match of the experimental spectra in the *r*-range of the first shell As–O signal with respect to both magnitude and imaginary part. Thus, even though the respective As(III) fractions were associated with considerable uncertainty and did not cause a substantial decrease in the *R*-factor (Table 5), they may nevertheless indicate that these samples contained traces of As(III). At the time of soil sampling, moisture in the soil profile was low and the soil was aerated. As(III) oxidation on partially Mn substituted Fe-oxides (Sun et al., 1999) or Mn-oxides (Oscarson et al., 1983) as well as As(III) co-oxidation with Fe(II) (Roberts et al., 2004) are expected to promote rapid As(III) oxidation during the aeration of previously reduced soil. It is therefore likely that soil As at the time of sample collection was predominantly As(V). However, we cannot exclude that further As(III) oxidation during soil drying and soil storage at room temperature.

Within experimental uncertainties, the As–Fe distances and coordination numbers obtained for the soil As spectra match the respective values of As(V) adsorbed to ferrihydrite (Table 4). On the other hand, it is still remarkable that the As–Fe distances of all soil samples were consistently higher than for As(V) adsorbed to ferrihydrite (Table 4). Considering the low As(III) fractions in the soil samples (Table 5), the seemingly longer As–Fe distances cannot be explained by As(III) adsorbed to ferrihydrite. On the other hand, the fitted distances approach those of amorphous ferric arsenate (3.36 Å) (Paktunc et al., 2003) or scorodite (3.38 Å, Table 4). The As–Fe distances of soil As spectra might thus indicate that a fraction of the As(V) is present as ferric arsenate-type surface precipitate (Paktunc et al., 2003, 2004). While As(V) adsorbed to ferrihydrite in the rhizosphere is formed by the concomitant oxidation of ferrous iron and As(III), the reference ferrihydrite with adsorbed As(V) was synthesized by hydrolyzing ferric iron and adsorbing As(V). Interestingly, As–Fe distances of 3.36 Å were reported for As(V)-sorbed lepidocrocite obtained by the oxidation of As(V) sorbed green rust (Randall et al., 2001). Thus, the As–Fe distances observed for the soil samples might reflect partial formation of ferric arsenate-type surface precipitates during the concomitant oxidation and precipitation of As(III) with Fe(II). To the best of our knowledge, however, no As–Fe distances have been reported for As(V) sorbed to Fe(III)-(hydr)oxides synthesized via the oxidation of Fe(II) and As(III) containing solutions. Alternatively, ferric arsenate-type surface precipitates might also form during the aging of As(V) adsorbed on ferrihydrite (Waychunas et al., 1993; Jia et al., 2006). No transformation of adsorbed As(V) was found at pH 8 over reaction times up to 7 weeks (Waychunas et al., 1993; Jia

Table 5
Soil As oxidation state from linear combination fits (LCF) of soil EXAFS spectra over *k*-range 3–11 $Å^{-1}$ using reference spectra of As(V) and As(III) adsorbed to ferrihydrite

Sample	Only As(V)[a]		As(V) and As(III)[b]		
	Fh–As(V)	*R*-factor[c]	Fh–As(V)	Fh–As(III)	*R*-factor[c]
Soil 0–15 cm	100% (±1%)	0.0142	99% (±1%)	3% (±2%)	0.0139
Soil 20–40 cm	101% (±2%)	0.0388	100% (±2%)	7% (±3%)	0.0375
Soil 70–80 cm	93% (±2%)	0.0509	90% (±2%)	13% (±3%)	0.0460
Rhizosphere	92% (±1%)	0.0190	89% (±1%)	13% (±2%)	0.0137
Matrix	98% (±1%)	0.0245	98% (±1%)	4% (±2%)	0.0242

[a] One-component LCF based on spectrum of As(V) adsorbed to ferrihydrite.
[b] Two-component LCF based on spectra of As(V) and As(III) adsorbed to ferrihydrite.
[c] *R*-factor = $\sum(\text{data-fit})^2/\sum\text{data}^2$.

et al., 2006). However, based on X-ray diffraction analysis and infrared spectroscopy, adsorbed As(V) on ferrihydrite was found to partly transform into ferric arsenate at pH 3–5 and over 2 weeks of aging at room temperature (Jia et al., 2006, 2007). Thus, the As–Fe distances observed in the soil samples (Table 4) might indicate that concomitant oxidation of Fe(II) and As(III) and adsorption of As(V) onto precipitating ferrihydrite are followed by the partial transformation of adsorbed As(V) to a ferric-arsenate type surface precipitate.

3.8. Influence of the plant roots on the speciation and distribution of As

The element distribution maps (Figs. 1 and 2) and the contents of As in manually separated rhizosphere and matrix soil (Table 2) clearly show that As in the studied soil is highly concentrated in the Fe-enrichments around the plant roots. From the correlation of As and Fe in the element distribution maps, the oxalate extractions (Tables 1 and 2) and the analysis of the XANES and EXAFS data (Figs. 3, 4, 7 and Table 4), we conclude that most soil As was As(V) associated with ferrihydrite. Recent studies on the speciation of As in Fe-plaque of *P. arundinacea*, *T. latifolia*, and *Oryza sativa* also showed that most As was associated with ferrihydrite (Hansel et al., 2002; Blute et al., 2004; Liu et al., 2006). The reported As(III) fractions (18–29%) were higher than those determined in the present study (Table 5), which may be attributable to permanently waterlogged conditions in the investigated systems. In contrast, the riparian floodplain soil studied in this work is only periodically flooded and was well aerated at the time of sample collection.

In the investigated floodplain soil, rusty Fe-enrichments extending into the soil around plant roots were clearly visible. Blackish Mn-concretions were sometimes observed close to the root channel surface. Localized Mn-enrichments close to the surface of root channels were also visible in the element distribution maps collected on thin sections from the subsoil and the topsoil (Figs. 1 and 2). In agreement with these observations, a study on Fe/Mn-concretions around roots of salt marsh plants showed that Mn-enrichment occurred closer to the root surface than Fe-accumulation (Caetano and Vale, 2002). The element distribution maps (Figs. 1 and 2) show that As is closely correlated with Fe-enrichments around root channels, but not with Mn-concretions. These trends are in agreement with studies on the sequestration of As in layered Fe/Mn crusts of marine nodules (Marcus et al., 2004b) and in Fe/Mn layers of lake sediments (Müller et al., 2002), which report a strong correlation of As with Fe, but not with Mn. The preferred association of As with Fe-oxides may reflect a higher adsorption affinity of As for Fe- than for Mn-oxides. However, the accumulation of As with Fe(III)-(hydr)oxides is more likely controlled by other factors, including (i) the stability ranges of Mn- and Fe-oxides and the dominant As oxidation state under variable Eh and pH conditions (Masscheleyn et al., 1991), (ii) the kinetics of Mn, Fe, and As oxidation reactions, and (iii) the spatial gradients in dissolved O_2, Fe^{2+}, Mn^{2+}, As(III), and As(V) between the reduced soil matrix and the O_2-releasing surfaces of roots under waterlogged conditions. Already mildly reducing conditions lead to the reductive dissolution of Mn-oxides, while As(V) and Fe(III)-(hydr)oxides are still stable (Masscheleyn et al., 1991). Thus, As(V) released from dissolving Mn-oxides may readsorb to Fe-oxides and other soil minerals in the soil matrix. At the same time, Mn^{2+} may be transported towards roots either by diffusion or by advective water flow caused by the transpiration of plants. The slow homogeneous oxidation of Mn^{2+} with O_2 and the catalytic oxidation of Mn^{2+} on Mn-oxide surfaces (Hem, 1981; Stumm and Morgan, 1996) explain the formation of Mn-rich nodules near the surfaces of root channels. Under more reducing conditions, the reductive dissolution of Fe(III)-(hydr)oxides and the reduction of As(V) to As(III) lead to an increase of the dissolved concentrations of Fe^{2+} and As(III) in the reduced soil matrix (Masscheleyn et al., 1991). By diffusion and transpiration water flow, dissolved Fe^{2+} and As(III) are transported towards plant roots. Because the oxidation of Fe^{2+} with O_2 proceeds more rapidly and at lower redox potential than the oxidation of Mn^{2+} (Stumm and Morgan, 1996), Fe-oxides already precipitate at lower O_2 partial pressures and further away from root channels than Mn-oxides. At the same time, the oxidation of As(III) to As(V) may be catalyzed by the oxidation of Fe^{2+} (Roberts et al., 2004) or by traces of Mn coprecipitated with Fe(III)-(hydr)oxides (Sun et al., 1999). Coprecipitation of As(III/V) with freshly forming or adsorption to already existing Fe(III)-(hydr)oxides may prevent further As(III) diffusion towards the root surface and its oxidation and uptake by discrete Mn-oxides.

From the total As contents in hand-picked rhizosphere and matrix soil from three undisturbed blocks of subsoil material, the fraction of As associated with Fe-enrichments around roots was estimated to account for 42%, 48%, and 72% of the total As in the studied soil volumes. While further analyses are needed to reliably quantify the As fraction in the rhizosphere, our results suggest that about half of the total As in the subsoil may be associated with Fe-enrichments around root channels. For plants grown in salt marshes, the fraction of As associated with the rhizosphere (including rhizosphere soil, Fe-plaque, and root tissues) in the topsoil (<20 cm) was reported to range from 3% to 19% of the total As (Otte et al., 1995; Doyle and Otte, 1997). Since the subsoil at our site was cemented by Fe-enrichments around root channels, the separation between rhizosphere and matrix soil may have been more accurate than in the latter studies, partly explaining the higher fractions of As associated with the rhizosphere. In addition, differences in root density will strongly affect the extent of As sequestration into the rhizosphere. We did not attempt to isolate rhizosphere and matrix soil in an undisturbed topsoil sample, because the higher organic carbon content and root density compared to the subsoil prevented to visually distinguish rhizosphere and matrix soil. However, the element distribution map collected around a root in the topsoil (Fig. 2) suggests that Fe and As are also enriched around roots in the topsoil.

At the studied site, the vegetation is dominated by perennial grasses and flowering plants. Thus, roots in the subsoil may exist for several years, allowing the formation

of massive Fe-enrichments extending up to several mm into the soil matrix. At the same time, the roots also increase the organic carbon content in the rhizosphere (Marschner, 1995). During a severe flood, the vegetation may be covered with water, leading to a decrease or stop of O_2 supply to the roots and the partial dissolution of the Fe-(hydr)oxides. However, such situations are rare. More likely, roots and the organic substance in the surrounding rhizosphere will become decomposed once the respective plant dies. Under waterlogged conditions, this will result in the reductive dissolution of Fe-(hydr)oxides and the release of Fe(II) and As(III/V). We therefore assume that the observed As- and Fe-enrichments may persist for several years, but that the dissolution of old Fe-enrichments under waterlogged conditions and the simultaneous formation of new ones lead to a continuous redistribution of Fe and As within the rooted subsoil.

3.9. Implications for the bioavailability and mobility of As in floodplain soils

In the riparian floodplain at Muldenstein, we find that high concentrations of As are accumulated in the subsoil rhizosphere. The μ-XRF analyses show that Fe and As are also strongly enriched around plant roots in the topsoil (Fig. 2). Because root density in the subsoil is much lower than in the topsoil, plant As uptake from the topsoil is likely more relevant than from the subsoil. Numerous recent studies showed that the formation of Fe-plaque on the surface of rice roots leads to the sequestration of As and to a reduction of the As transfer to the rice shoots and grains (Abedin et al., 2002a,b; Liu et al., 2004a,b; Chen et al., 2005; Hu et al., 2005). These studies were either carried out with plants grown in nutrient solution (hydroponic studies) or with homogenized soil (pot experiments). Pot experiments with homogenized soil may approximate the conditions in annually puddled and homogenized paddy soils. In riparian soils and constructed wetlands, however, the accumulation of As and Fe in the rhizosphere may persist over several years. The association of As with Fe-(hydr)oxides in the rhizosphere and the Fe-plaque may reduce the availability of As for plant uptake. On the other hand, the massive accumulation of As close to the plant roots might also increase the uptake of As by plants relative to the same soil with a homogeneous As and Fe distribution. Thus, the spatial distribution of As and its association with Fe-(hydr)oxides in the rhizosphere should be considered in studies on the As-uptake of plants grown in natural and constructed wetlands.

Studies on vegetated and non-vegetated salt marshes showed that higher levels of As were accumulated (or retained) in vegetated plots (Doyle and Otte, 1997). From studies on the sequestration of As into the Fe-plaque of wetland plants, it was concluded that this process may lead to a substantial attenuation of As and that disruption of the vegetation might promote reductive As remobilization (Hansel et al., 2002; Blute et al., 2004). In the floodplain at Muldenstein, we estimate from our results that about half of the As in the rooted subsoil is associated with Fe-(hydr)oxides enriched in the rhizosphere. If the extent of As sequestration is similar in the topsoil, roughly half of the As in the rooted soil depth is sorbed to Fe(III)-(hydr)oxides in the rhizosphere. Thus, plants growing at the site may limit the mobility of As under waterlogged conditions. If the vegetation is impaired or removed, the O_2 supply to the soil during periods of high ground water levels or flooding will be reduced or stopped. The reductive dissolution of Fe-(hydr)oxides in combination with As(V) reduction to As(III) might then lead to leaching of As from the soil profile. These processes must be taken into account for the management of contaminated riparian soils.

ACKNOWLEDGMENTS

We thank Stefan Mangold (ANKA) and Matthew A. Marcus (ALS) for their help during data acquisition at synchrotron light sources. Jakob Frommer and Olivier Jacquat (ETH Zurich) are acknowledged for their valuable input with respect to the EXAFS data analysis. We thank Kurt Barmettler (ETH Zurich) for his support in the laboratory. Prof. Elias Landolt (ETH Zurich) kindly helped with the identification of the dominant plant species. Synthetic lepidocrocite was provided by Paul Borer (ETH Zurich). Three anonymous reviewers and the associate editor Prof. Peggy O'Day are thanked for their constructive comments on an earlier version of this manuscript. The Angströmquelle Karlsruhe GmbH (ANKA, Karlsruhe, Germany) is acknowledged for providing beamtime at the XAS beamline and the Advanced Light Source (ALS, Berkeley, USA) for beamtime at the microfocused beamline 10.3.2. The ALS is supported by the Director, Office of Science, Office of Basic Energy Sciences, Materials Sciences Division, of the U.S. Department of Energy under Contract No. DE-AC03-76SF00098 at Lawrence Berkeley National Laboratory. This research was partly funded by the Swiss State Secretariat for Education and Research (SER) as a contribution to the EU project AQUATERRA (6th EU RTD framework program, Contract No. 505428).

REFERENCES

Abedin M. J., Cotter-Howells J. and Meharg A. A. (2002a) Arsenic uptake and accumulation in rice (*Oryza sativa* L.) irrigated with contaminated water. *Plant Soil* **240**, 311–319.

Abedin M. J., Cresser M. S., Meharg A. A., Feldmann J. and Cotter-Howells J. (2002b) Arsenic accumulation and metabolism in rice. *Environ. Sci. Technol.* **36**, 962–968.

Ankudinov A. L. and Rehr J. J. (2000) Theory of solid-state contributions to the X-ray elastic scattering amplitude. *Phys. Rev. B* **62**, 2437–2445.

Arai Y., Elzinga E. J. and Sparks D. L. (2001) X-ray absorption spectroscopic investigation of arsenite and arsenate adsorption at the aluminum oxide-water interface. *J. Colloid Interface Sci.* **235**, 80–88.

Arai Y. and Sparks D. L. (2002) Residence time effects on arsenate surface speciation at the aluminum oxide–water interface. *Soil Sci.* **167**, 303–314.

Arai Y., Sparks D. L. and Davis J. A. (2004) Effects of dissolved carbonate on arsenate adsorption and surface speciation at the hematite–water interface. *Environ. Sci. Technol.* **38**, 817–824.

Beaulieu B. T. and Savage K. S. (2005) Arsenate adsorption structures on aluminum oxide and phyllosilicate mineral surfaces in smelter-impacted soils. *Environ. Sci. Technol.* **39**, 3571–3579.

Blute N. K., Brabander D. J., Hemond H. F., Sutton S. R., Newville M. G. and Rivers M. L. (2004) Arsenic sequestration

by ferric iron plaque on cattail roots. *Environ. Sci. Technol.* **38**, 6074–6077.

Borer P. M., Sulzberger B., Reichard P. and Kraemer S. M. (2005) Effect of siderophores on the light-induced dissolution of colloidal iron(III) (hydr)oxides. *Marine Chem.* **93**, 179–193.

Brandt O. 2003. Eintrags- und Wirkungspfade von Schwermetallen und Arsen in Flußaue-Systemen am Beispiel der Mulde zwischen Bitterfeld/Wolfen und Dessau, Sachsen-Anhalt. Ph.D, Technische Universität Berlin.

Caetano M. and Vale C. (2002) Retention of arsenic and phosphorus in iron-rich concretions of Tagus salt marshes. *Marine Chem.* **79**, 261–271.

Cancès B., Juillot F., Morin G., Laperche V., Alvarez L., Proux O., Hazeman J.-L., Brown G. E. and Calas G. (2005) XAS evidence of As(V) association with iron oxyhydroxides in a contaminated soil at a former arsenical pesticide processing plant. *Environ. Sci. Technol.* **39**, 9398–9405.

Chen Z., Zhu Y.-G., Liu W.-J. and Meharg A. A. (2005) Direct evidence showing the effect of root surface iron plaque on arsenite and arsenate uptake into rice (*Oryza sativa*) roots. *New Phytologist.* **165**, 91–97.

Dixit S. and Hering J. G. (2003) Comparison of arsenic(V) and arsenic(III) sorption onto iron oxide minerals: implications for arsenic mobility. *Environ. Sci. Technol.* **37**, 4182–4189.

Doyle M. O. and Otte M. L. (1997) Organism-induced accumulation of iron, zinc and arsenic in wetland soils. *Environ. Pollut.* **96**, 1–11.

FAO. (2006a) Guidelines for Soil Description. Food and Agriculture Organization of the United Nations, Rome, Rome.

FAO. (2006b) World Reference Base for Soil Resources 2006 World Soil Resources Reports No. 103. Food and Agriculture Organization of the United Nations, Rome, Rome.

Farquhar M. L., Charnock J. M., Livens F. R. and Vaughan D. J. (2002) Mechanisms of arsenic uptake from aqueous solution by interaction with goethite, lepidocrocite, mackinawite, and pyrite: an X-ray absorption spectroscopy study. *Environ. Sci. Technol.* **36**, 1757–1762.

Fendorf S. E., Eick M. J., Grossl P. and Sparks D. L. (1997) Arsenate and chromate retention mechanisms on goethite: 1. Surface structure. *Environ. Sci. Technol.* **31**, 315–320.

Foster A., Brown G. E. and Parks G. A. (2003) X-ray absorption fine structure study of As(V) and Se(IV) sorption complexes on hydrous Mn oxides. *Geochim. Cosmochim. Acta* **67**, 1937–1953.

Foster A. L., Brown G. E., Tingle T. N. and Parks G. A. (1998) Quantitative arsenic speciation in mine tailings using X-ray absorption spectroscopy. *Am. Mineralogist* **83**, 553–568.

Fuller C. C., Davis J. A. and Waychunas G. A. (1993) Surface chemistry of ferrihydrite: Part 2. Kinetics of arsenate adsorption and coprecipitation. *Geochim. Cosmochim. Acta* **57**, 2271–2282.

Geller W., Ockenfeld K., Böhme M. and Knöchel, A. (2004) Schadstoffbelastung nach dem Elbe-Hochwasser 2002. UFZ - Umweltforschungszentrum Leipzig-Halle GmbH, Magdeburg.

Goldberg S. (2002) Competitive adsorption of arsenate and arsenite on oxides and clay minerals. *Soil Sci. Soc. Am. J.* **66**, 413–421.

Goldberg S. and Johnston C. T. (2001) Mechanisms of arsenic adsorption on amorphous oxides evaluated using macroscopic measurements, vibrational spectroscopy, and surface complexation modeling. *J. Colloid Interface Sci.* **234**, 204–216.

Hansel C. M., Fendorf S., Sutton S. and Newville M. (2001) Characterization of Fe plaque and associated metals on the roots of mine-waste impacted aquatic plants. *Environ. Sci. Technol.* **35**, 3863–3868.

Hansel C. M., La Force M. J., Fendorf S. and Sutton S. (2002) Spatial and temporal association of As and Fe species with aquatic plant roots. *Environ. Sci. Technol.* **36**, 1988–1994.

Hem J. D. (1981) Rates of manganese oxidation in aqueous systems. *Geochim. Cosmochim. Acta* **45**, 1369–1374.

Hsu P. H. and Sikora F. (1993) Effects of aluminum and phosphate concentrations and acidity on the crystallization of variscite at 90 °C. *Soil Sci.* **156**, 71–78.

Hu Y., Li Y. G., Zhu Y.-G., Huang Y.-Z., Hu H.-Q. and Christie P. (2005) Sequestration of As by iron plaque on the roots of three rice (*Oryza sativa* L.) cultivars in a low-P soil with or without P fertilizer. *Environ. Geochem. Health* **27**, 169–176.

Hudson E. A., Allen P. G., Terminello L. J., Denecke M. A. and Reich T. (1996) Polarized X-ray-absorption spectroscopy of the uranyl ion: comparison of the experiment and theory. *Phys. Rev. B* **54**, 156–165.

Inskeep W. P., McDermott T. R. and Fendorf S. (2002) Arsenic (V)/(III) cycling in soils and natural waters: chemical and microbiological processes. In *Environmental Chemistry of Arsenic* (ed. W. T. Frankenberger). Marcel Dekker Inc., New York.

Jia Y., Xu L., Fang Z. and Demopoulos G. P. (2006) Observation of surface precipitation of arsenate on ferriyhdrite. *Environ. Sci. Technol.* **39**, 3571–3579.

Jia Y., Xu L., Wang X. and Demopoulos G. P. (2007) Infrared spectroscopic and X-ray diffraction characterization of the nature of adsorbed arsenate on ferrihydrite. *Geochim. Cosmochim. Acta* **71**, 1643–1654.

Kalbitz K. and Wennrich R. (1998) Mobilization of heavy metals and arsenic in polluted wetland soils and its dependence on dissolved organic matter. *Sci. Total Environ.* **209**, 27–39.

Kirk G. (2004) *The Biogeochemistry of Submerged Soils*. John Wiley & Sons Ltd., Chichester.

Kitahama K., Kiriyama R. and Baba Y. (1975) Refinement of crystal-structure of scorodite. *Acta Crystallogr. B* **31**, 322–324.

Klemm W., Greif A., Broekaert J. A. C., Siemens V., Junge F. W., van der Veen A., Schultze M. and Duffek A. (2005) A study on arsenic and the heavy metals in the Mulde river system. *Acta Hydrochim. Hydrobiol.* **33**, 475–491.

Ladeira A. C. Q., Ciminelli V. S. T., Duarte H. A., Alves M. C. M. and Ramos A. Y. (2001) Mechanism of anion retention from EXAFS and density functional calculations: arsenic(V) adsorbed on gibbsite. *Geochim. Cosmochim. Acta* **65**, 1211–1217.

Lamers L. P. M., Loeb R., Antheunisse A. M., Miletto M., Lucassen E. C. H. E. T., Boxman A. W., Smolders A. J. P. and Roelofs J. G. M. (2006) Biogeochemical constraints on the ecological rehabilitation of wetland vegetation in river floodplains. *Hydrobiologia* **565**, 165–186.

Liu W.-J., Zhu Y.-G., Smith F. A. and Smith S. E. (2004a) Do iron plaque and genotypes affect arsenate uptake and translocation by rice seedlings (*Oryza sativa* L.) grown in solution culture? *J. Exp. Bot.* **55**, 1707–1713.

Liu W.-J., Zhu Y.-G., Smith F. A. and Smith S. E. (2004b) Do phosphorus nutrition and iron plaque alter arsenate (As) uptake by rice seedlings in hydroponic culture? *New Phytologist* **162**, 481–488.

Liu W. J., Zhu Y. G., Hu Y., Williams P. N., Gault A. G., Meharg A. A., Charnock J. M. and Smith F. A. (2006) Arsenic sequestration in iron plaque, its accumulation and speciation in mature rice plants (*Oryza sativa* L.). *Environ. Sci. Technol.* **40**, 5730–5736.

Manceau A. and Combes J. M. (1988) Structure of Mn and Fe oxides and oxyhydroxides: a topological approach by EXAFS. *Phys. Chem. Miner.* **15**, 283–295.

Manceau A. and Gates W. P. (1997) Surface structural model for ferrihydrite. *Clays Clay Miner.* **45**, 448–460.

Manning B. (2005) Arsenic speciation in As(III)- and As(V)-treated soil using XANES spectroscopy. *Microchim. Acta* **151**, 181–188.

Manning B. A., Fendorf S. E., Bostick B. and Suarez D. L. (2002) Arsenic(III) oxidation and arsenic(V) adsorption reactions on synthetic birnessite. *Environ. Sci. Technol.* **36**, 976–981.

Marcus M. A., Macdowell A. A., Celestre R. S., Manceau A., Miller T., Padmore H. A. and Sublett R. E. (2004a) Beamline 10.3.2 at ALS: a hard X-ray microprobe for environmental and materials sciences. *J. Synchrotron Radiat.* **11**, 239–247.

Marcus M. A., Manceau A. and Kersten M. (2004b) Mn, Fe, Zn, and As speciation in a fast-growing ferromanganese marine nodule. *Geochim. Cosmochim. Acta* **68**, 3125–3136.

Marschner H. (1995) *Mineral Nutrition of Higher Plants*. Academic Press, London.

Martell A. E., Smith R. M. and Motekaitis R. J. (1997) NIST Database 46, Critically Selected Stability Constants of Metal Complexes, Version 6.0. National Institute of Standards and Technology, Gaithersburg, MD, USA.

Masscheleyn P. H., Delaune R. D. and Patrick W. H. (1991) Effect of redox potential and pH on arsenic speciation and solubility in a contaminated soil. *Environ. Sci. Technol.* **25**, 1414–1419.

McGeehan S. L. and Naylor D. V. (1994) Sorption and redox transformation of arsenite and arsenate in two flooded soils. *Soil Sci. Soc. Am. J.* **58**, 337–342.

Morin G., Lecocq D., Juillot F., Calas G., Ildefonse P., Belin S., Briois V., Dillmann P., Chevallier P., Gauthier C., Sole A., Petit P. E. and Borensztajn S. (2002) EXAFS evidence of sorbed arsenic(V) and pharmacosiderite in a soil overlying the Echassières geochemical anomaly, Allier, France. *Bull. Soc. Geol. France* **173**, 281–291.

Müller B., Granina L., Schaller T., Ulrich A. and Wehrli B. (2002) P, As, Sb, Mo, and other elements in sedimentary Fe/Mn layers of lake Baikal. *Environ. Sci. Technol.* **36**, 411–420.

O'Reilly S. E., Strawn D. G. and Sparks D. L. (2001) Residence time effects on arsenate adsorption/desorption mechanisms on goethite. *Soil Sci. Soc. Am. J.* **65**, 67–77.

Ona-Nguema G., Morin G., Juillot F., Calas G. and Brown G. E. (2005) EXAFS analysis of arsenite adsorption onto two-line ferrihydrite, hematite, goethite, and lepidocrocite. *Environ. Sci. Technol.* **39**, 9147–9155.

Onken B. M. and Hossner L. R. (1996) Determination of arsenic species in soil solution under flooded conditions. *Soil Sci. Soc. Am. J.* **60**, 1385–1392.

Oscarson D. W., Huang P. M., Liaw W. K. and Hammer U. T. (1983) Kinetics of oxidation of arsenite by various manganese dioxides. *Soil Sci. Soc. Am. J.* **47**, 644–648.

Otte M. L., Kearns C. C. and Doyle M. O. (1995) Accumulation of arsenic and zinc in the rhizosphere of wetland plants. *Bull. Environ. Contam. Toxicol.* **55**, 154–161.

Paktunc D., Foster A., Heald S. and Laflamme G. (2004) Speciation and characterization of arsenic in gold ores and cyanidation tailings using X-ray absorption spectroscopy. *Geochim. Cosmochim. Acta* **68**, 969–983.

Paktunc D., Foster A. and Laflamme G. (2003) Speciation and characterization of arsenic in Ketza river mine tailings using X-ray absorption spectroscopy. *Environ. Sci. Technol.* **37**, 2067–2074.

Penrose W. R. (1974) Arsenic in the marine and aquatic environments: analysis, occurence, and significance. *CRC Crit. Rev. Environ. Control* **4**, 465–482.

Pierce M. L. and Moore C. B. (1982) Adsorption of arsenite and arsenate on amorphous iron hydroxide. *Water Res.* **16**, 1247–1253.

Ponnamperuma F. N. (1972) The chemistry of submerged soils. *Adv. Agronomy* **24**, 29–96.

Randall S. R., Sherman D. M. and Ragnarsdottir K. V. (2001) Sorpion of As(V) on green rust ($Fe_4(II)Fe_2(III)(OH)_{12}SO_4$* $3H_2O$) and lepidocrocite (gamma-FeOOH): surface complexes from EXAFS spectroscopy. *Geochim. Cosmochim. Acta* **65**, 1015–1023.

Ravel B. and Newville M. (2005) ATHENA, ARTEMIS, HEPHAESTUS: data analysis for X-ray absorption spectroscopy using IFEFFIT. *J. Synchrotron Radiat.* **12**, 537–541.

Roberts L. C., Hug S. J., Ruettimann T., Billah M. M., Khan A. W. and Rahman M. T. (2004) Arsenic removal with iron(II) and iron(III) in waters with high silicate and phosphate concentrations. *Environ. Sci. Technol.* **38**, 307–315.

Schwertmann U. and Cornell R. M. (1991) *Iron Oxides in the Laboratory*. VCH Verlagsgesellschaft, Weinheim.

Scott M. J. and Morgan J. J. (1995) Reactions at oxide surfaces. 1. Oxidation of As(III) by synthetic birnessite. *Environ. Sci. Technol.* **29**, 1995.

Sherman D. M. and Randall S. R. (2003) Surface complexation of arsenic(V) to iron(III) (hydr)oxides: structural mechanism from ab initio molecular geometries and EXAFS spectroscopy. *Geochim. Cosmochim. Acta* **67**, 422–4230.

Stern E. A., Newville M., Ravel B., Yacoby Y. and Haskel D. (1995) The UWXAFS analysis package: philosophy and details. *Phys. B* **208 and 209**, 117–120.

Stumm W. and Morgan J. J. (1996) *Aquatic Chemistry*. John Wiley, New York.

Sun X., Doner H. E. and Zavarin M. (1999) Spectroscopic study of arsenite [As(III)] oxidation on Mn-substituted goethite. *Clays Clay Miner.* **47**, 474–480.

Vink J. P. M. (2002) Measurement of heavy metal speciation over redox gradients in natural water—sediment interfaces and implications for uptake by benthic organisms. *Environ. Sci. Technol.* **36**, 5130–5138.

Violante A. and Pigna M. (2002) Competitive sorption of arsenate and phosphate on different clay minerals and soils. *Soil Sci. Soc. Am. J.* **66**, 1788–1796.

Waltham C. A. and Eick M. J. (2002) Kinetics of arsenic adsorption on goethite in the presence of sorbed silicic acid. *Soil Sci. Soc. Am. J.*, 66.

Waychunas G. A., Rea B. A., Fuller C. C. and Davis J. A. (1993) Surface chemistry of ferrihydrite: Part 1. EXAFS studies of the geometry of coprecipitated and adsorbed arsenate. *Geochim. Cosmochim. Acta* **57**, 2251–2269.

Wenzel W. W., Kirchbaumer N., Prohaska T., Stingeder G., Lombi E. and Adriano D. C. (2001) Arsenic fractionation in soils using an improved sequential extraction procedure. *Analyt. Chim. Acta* **436**, 309–323.

Wijnhoven S., van der Veelde G., Leuven R. S. E. W., Eijsackers H. J. P. and Smits A. J. M. (2006) Metal accumulation risks in regularly flooded and non-flooded parts of floodplains of the river Rhine: Extractability and exposure through the food chain. *Chem. Ecol.* **22**, 463–477.

Associate editor: Peggy A. O'Day